ACADEMIC PRESS

Available online at www.sciencedirect.com
SCIENCE DIRECT®

Journal of Catalysis 216 (2003) 223–235

JOURNAL OF CATALYSIS

www.elsevier.com/locate/jcat

# Preparation and characterization of model catalysts: from ultrahigh vacuum to in situ conditions at the atomic dimension

H.-J. Freund,* M. Bäumer, J. Libuda, T. Risse, G. Rupprechter, and S. Shaikhutdinov

*Fritz-Haber-Institut der Max-Planck-Gesellschaft, Faradayweg 4-6, D-14195 Berlin, Germany*

Received 9 July 2002; revised 19 September 2002; accepted 30 September 2002

**Abstract**

In situ characterization and reaction studies of working catalytic systems are an issue of current interest. We present studies on well characterized model systems, i.e., deposited metal nanoparticles, applying a variety of experimental techniques in an attempt to bridge gaps between surface science and catalysis. In particular, we investigate methanol dehydrogenation and ethene hydrogenation under UHV as well as ambient conditions and apply nonlinear optical techniques. We use electron spin resonance to study intermediately formed radicals in Ziegler–Natta polymerization of ethene. It is concluded that there is a chance to transfer results from studies on model systems toward an understanding of catalysis.


*Keywords:* Model catalysts; In-situ studies; Sum frequency generation; Electron spin resonance; Ethene hydrogenation; Ethene polymerization; Methanol dehydrogenation

## 1. Introduction

A characteristic of working heterogeneous catalysts is their complexity [1,2]. These systems are complex with respect to structure and chemical stoichiometry as well as reaction kinetics. In recent years, therefore, strong efforts have been undertaken to prepare and characterize model catalyst systems. Such systems encompass some of the degrees of complexity of the real system in an attempt to isolate those and study their influence on chemical reactivity of the system under both ideal ultra-high-vacuum conditions, as well as under ambient atmospheric conditions [3–10].

In the present review two types of model systems are discussed: dispersed metal catalysts for hydrogenation and dehydrogenation reactions [11–13], and a model system where a homogeneous catalyst has been heterogenized by grafting it on a substrate, i.e., a Ziegler–Natta low-pressure ethene polymerization model catalyst [14]. As we are interested in comparing reactivities under UHV and ambient conditions, results obtained with a variety of experimental methods need to be consulted. We will have to refer to the literature for an introduction into the physical basis of some of them.

## 2. Experimental

The experiments were performed in a variety of ultra-high vacuum systems built and situated at the Fritz Haber Institute of the Max Planck Society in Berlin. For details please consult the following references: For preparation of dispersed metal model systems see Ref. [15]. For preparation of Ziegler–Natta model systems see Ref. [16]. At this point already we also refer to articles summarizing some of the more specific experimental techniques relating to the data presented in this review. For sum-frequency generation we refer to Refs. [17–19]. For electron spin resonance as applied to surface studies we refer to [20,21].

## 3. Models for dispersed metal catalysts

In a technical catalyst, a catalytically active component such as a transition metal is dispersed over a suitable support material—usually an oxide like alumina or silica. In the first place, this is done in order to achieve the highest possible surface area of the active phase. Because of the high degree of dispersion, however, particle size effects originating from specific structural or electronic features and metal substrate interactions can influence the catalytic behaviour significantly. Of course, it has always been a central question

* Corresponding author.
*E-mail address:* freund@fhi-berlin.mpg.de (H.-J. Freund).

0021-9517/03/$ – see front matter 
doi:10.1016/S0021-9517(02)00073-8

in catalytic research how these effects can be exploited to improve the catalytic activity or the selectivity of a supported catalyst [1].

Nevertheless, there is still only very limited fundamental knowledge about the relationship and the interplay between structure, adsorption behavior, and chemical or catalytic activity of small deposited metal aggregates. Since the complex structure of real catalysts often hampers the attempt to connect macroscopic effects with the microscopic processes taking place on the surface, an increasing number of model studies have been conducted so far to tackle these questions.

Recently, a number of reviews concerning the "surface science approach" have been published taking a critical look at the different strategies to compose and explore model catalysts [3–10]. Advances in catalysis has dedicated an entire issue to this area recently. The spectrum ranges from studies based on polycrystalline or amorphous oxide substrates [3] to investigations on oxide single crystals or well-ordered films [4–8,10]. Also, with respect to the preparation of the particles, different concepts have been proposed. One approach is to apply techniques which come as close as possible to industrial catalyst manufacture like wet impregnation or exchange in solution [3]. Unfortunately, this often involves the disadvantage that structure and morphology of the deposits are rather difficult to control. Thus, vapor deposition of metals [4–10] or deposition of metal clusters from the gas phase [22] under UHV conditions have been preferred in experiments keyed to more fundamental questions about the correlation between structure and properties of small metal particles.

In this context, ultrathin oxide films grown on a metallic substrate are an excellent choice to circumvent problems [4–10] connected with the insulating nature of some bulk oxides. It has been shown that even films with a thickness of just a few ångstoms can exhibit physical properties characteristic of the bulk material [23]. Various groups extensively explored preparation techniques based on the evaporation of a metal (or nonmetal) onto a host crystal—mostly a refractory metal—in an ambient oxygen atmosphere [6,7,24–26]. Another promising possibility is the oxidation of a suitable alloy sample containing the metal which should be oxidized. A well-known example of that kind is the formation of well-ordered thin alumina films on the low-index surfaces of certain Al alloys [27–33]. But it is not unlikely that this approach also works in other cases [34]. An overview of some well-ordered thin oxide films described in the literature can be found in Ref. [15].

In Fig. 1 we show results on an alumina-based model system which has been prepared by oxidation of an NiAl(110) surface and studied via STM in our laboratory [15].

The upper left panel (a) shows the clean alumina surface as imaged by a scanning tunneling microscope [28].

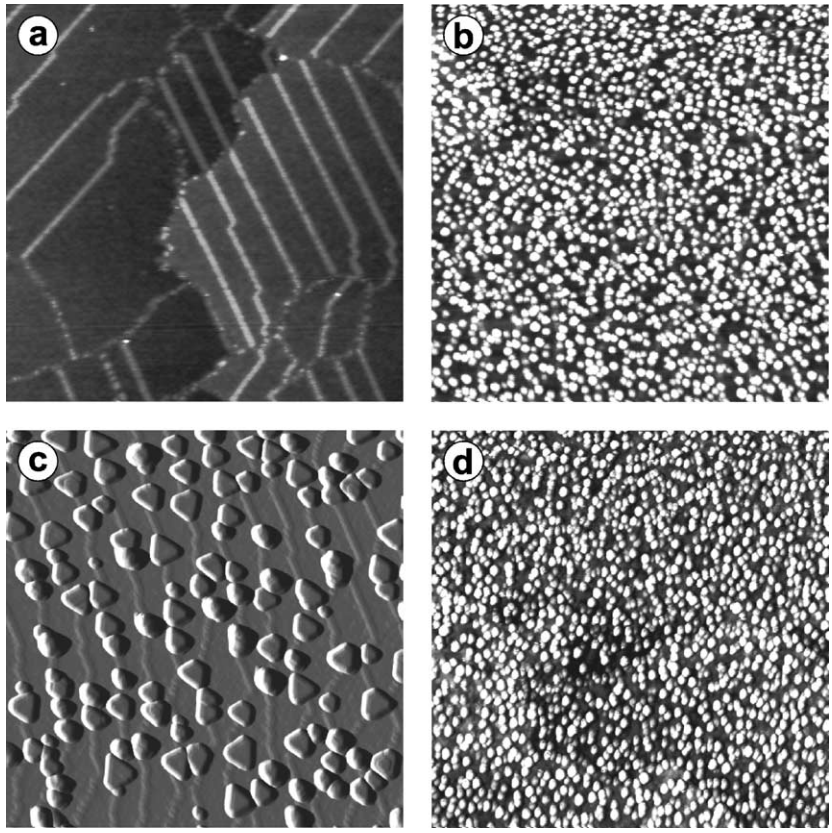


Fig. 1. Scanning tunneling images (1000 Å × 1000 Å) of (a) clean alumina film on NiAl(110); (b) 0.2-Å Pd deposited at 90 K; (c) 2-Å Pd deposited at 300 K; (d) 0.2-Å Pd deposited on the prehydroxylated film at 300 K.

The surface is well ordered and there are several kinds of defects on the surface. One type consists of reflection domain boundaries between the two growth directions of $Al_2O_3$(0001) on the NiAl(110) surface [27]. There are antiphase domain boundaries within the reflection domains, and, in addition, there are point defects which are not resolved in the images. The morphology does not change dramatically after the film is hydroxylated [35]. The additional panels show STM images of palladium deposits on the clean surface at low temperature (b) and at room temperature (c) [15,36], as well as an image after deposition of Pd on a hydroxylated substrate at room temperature (d) [37]. The amount deposited onto the hydroxylated surface is equivalent to the amount deposited onto the clean alumina surface at room temperature. Upon vapor deposition of Pd at low temperature, small particles (the protrusions shown in Fig. 1b) nucleate on the point defects of the substrate and a narrow distribution of sizes of particles is generated. If the deposition of Pd is performed at 300 K, the mobility of Pd atoms is considerably higher so that nucleation at the line defects of the substrate becomes dominant (features line up with the bright lines in Fig. 1c). Consequently, all the material nucleates on steps, reflection domains and antiphase domain boundaries. The particles have a relatively uniform size, in turn depending on the amount of material deposited. If the same amount of material is deposited onto a hydroxylated surface, the particles (the protrusions shown in Fig. 1d) are considerably smaller and distributed across the entire surface; i.e., a much higher metal dispersion is obtained, which is very similar to the dispersion found at 90 K [35].

The sintering process is an interesting subject. Research on this process is just beginning [15]. A more basic process is metal atom diffusion on oxide substrates. Diffusion studies [38] could profit from atomic resolution, once it is obtained for deposited aggregates on oxide surfaces. While for clean $TiO_2$ surfaces and a few other oxide substrates atomic resolution may be obtained routinely, there are few studies on deposited metal particles where atomic resolution has been reported [39]. A joint effort between Fleming Besenbacher and our group [40] has lead to atomically resolved images of Pd aggregates deposited on the thin alumina film. Fig. 2a shows such an image of an aggregate about 50 Å in width. The particle is crystalline and exposes on its top a (111) facet. Also, on the side, (111) facets, typical for a cuboctahedral particle, can be discerned.

The cluster on the oxide support is schematically represented in Fig. 2b. Terrace sites and edge, corner, and interface sites are differently shaded in order to make their specificity obvious. These “extra sites” in combination with the finite size of the facets render the situation on a cluster different from the one encountered on a single-crystal metal surface [18].

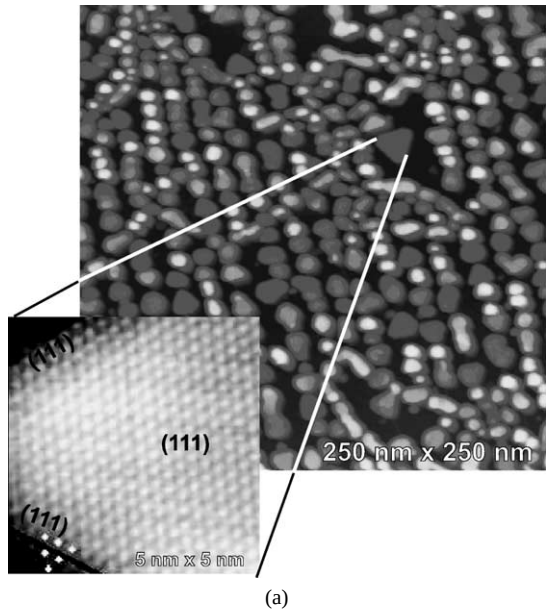


(a)

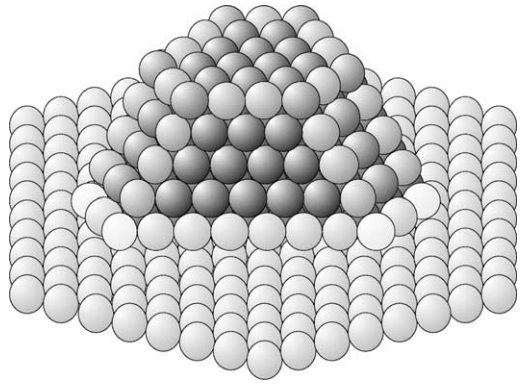

(b)

Fig. 2. (a) Scanning tunneling images of a room temperature Pd deposit on $Al_2O_3$/NiAl(110). The inset shows an individual deposit in atomic resolution [40]. (b) Schematic representation of a cubooctahedral metal cluster on a substrate.

### *3.1. Controlling selectivity through site specific reactions* [12]

In the following we summarize evidence for the specific activity (selectivity) of coexisting sites on a well-defined supported Pd–nanoparticle system discussed above. As a model reaction we choose the decomposition of methanol. For this reaction system two competing decomposition pathways exist (see Fig. 3): Whereas dehydrogenation to CO represents the dominant reaction channel [41,42], slow carbon–oxygen bond breakage leads to formation of adsorbed carbon and $CH_x$ species [42–44].

For the kinetic measurements we employ molecular beam techniques (e.g., [4,45–47]) which provide a unique way to derive detailed kinetic information. In order to perform such experiments we use a molecular beam system which allows to cross up to three beams on the sample surface and perform time-resolved reflection absorption IR

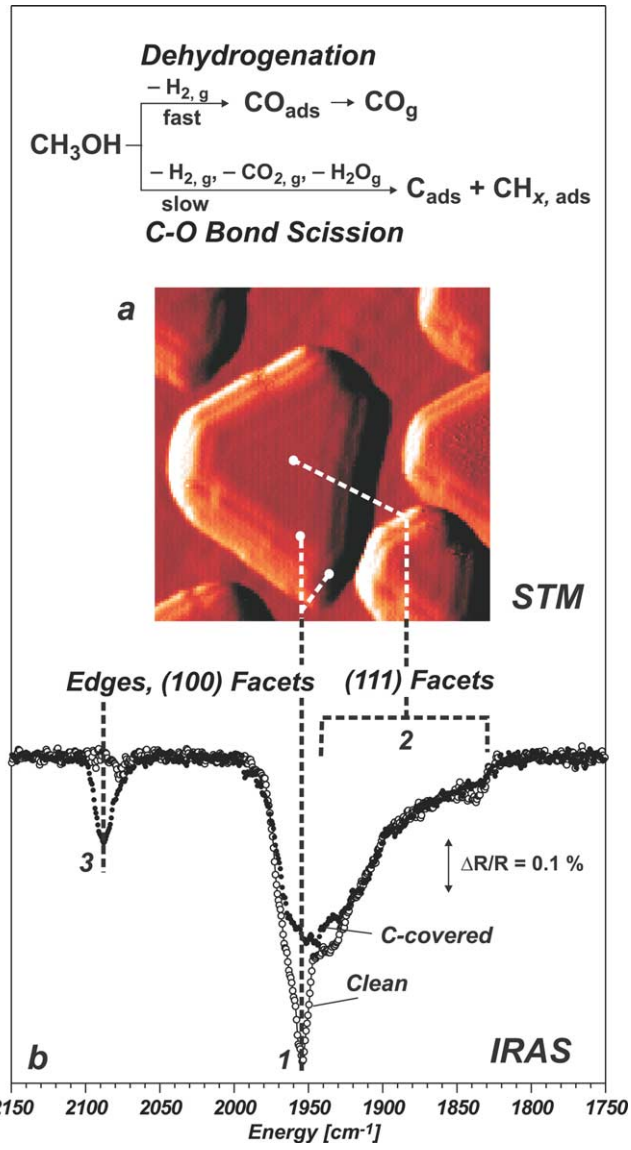


Fig. 3. Two competing reaction pathways for methanol decomposition on Pd particles supported on $Al_2O_3$/NiAl(110): fast dehydrogenation and slow C–O bond scission. (a) STM image of the Pd particles grown at 300 K (15 × 15 nm), from [108]; (b) IR reflection absorption spectra for CO adsorbed on Pd/$Al_2O_3$/NiAl (sample temperature 100 K, after CO exposure at 300 K). Open symbols: clean particles immediately after preparation; solid symbols: partially C-covered particles after prolonged exposure to methanol at 440 K.

spectroscopy (TR-RAIRS) and angle resolved/integrated gas phase detection, simultaneously [48]. Recently, we have applied the molecular beam approach to the CO oxidation on supported model catalysts [49,50].

Molecular adsorption of methanol is followed by the formation of methoxy species on the Pd particles. This first intermediate is stable up to temperatures of 200 K. At higher temperatures, decomposition proceeds via two competing reaction pathways. Dehydrogenation as the dominating reaction channel results in rapid formation of CO. Depending on the CO formation and desorption rate (i.e., the surface temperature), a significant steady state coverage of CO adsorbed on the Pd particles is built up, which can be monitored via in situ TR-RAIRS (IR at 440 K: $\tilde{\nu} = 1900$ cm$^{-1}$, 1840 cm$^{-1}$ (C=O)).

As a second pathway, we observe slow cleavage of the carbon–oxygen bond, leading to formation of adsorbed carbon and hydrocarbon species. This assumption is corroborated by two observations: First, weak features in the CH stretching frequency region indicate the presence of $CH_x$ species (IR: $\tilde{\nu} = 2945$ cm$^{-1}$, 2830 cm$^{-1}$ (C–H)). Such hydrocarbon species have been shown to be stable up to 500 K [43]. Second, in a TPD experiment we observe desorption of hydrocarbons (15 amu, 700 K) and recombinative desorption of CO (28 amu, 800 K), which is characteristic of the presence of atomic carbon [51].

It is essential to note that during CO exposure under identical conditions no carbon formation is observed on the same Pd particle system [49]. From this we infer that the carbon deposits do not originate from CO decomposition, but from breakage of the C–O bond during the dehydrogenation process.

The question arises of where on the nanoparticles (Fig. 3a) the carbon deposits are located. This question is answered by RAIRS using CO as a probe molecule. The corresponding spectra for the pristine Pd particles and after prolonged exposure to methanol are compared in Fig. 3b.

For the pristine sample (Fig. 3b, open symbols), the spectrum is dominated by a sharp absorption feature at 1960 cm$^{-1}$ (1) with a broad low-frequency shoulder (2) (1930 to 1840 cm$^{-1}$) and a additional weak feature at 2080 cm$^{-1}$ (3). Previously, the features between 1930 and 1840 cm$^{-1}$ (2) have been assigned to CO adsorbed on hollow sites on Pd(111), and the absorption peak at 2080 cm$^{-1}$ (3) to on-top CO on Pd(111) [18,52,53]. A detailed comparison with previous work shows that the prominent absorption band at 1960 cm$^{-1}$ (1) originates from a superposition of bridge-bonded CO on (100) facets and CO adsorbed at defect sites such as particle edges or steps [52,53]. The contribution of (100) facets, however, is expected to be small due to the minor fraction of these facets and their tilted geometry (as a consequence of the surface selection rule, IR absorption is attenuated on small tilted facets, e.g., [54]). Following these arguments, we assume that the absorption feature at 1960 cm$^{-1}$ is dominated by CO adsorbed on defect sites, mainly steps and particle edges (see Fig. 3). This is further corroborated by SFG data of CO on Pd(111) surfaces where this peak dominates after deliberately production of defects by sputtering [18]. Note, however, that the signals are expected to be strongly modified by dipole coupling effects [55]. As a consequence, the relative intensities do not directly reflect the relative abundance of the corresponding sites. In particular, the defect feature at high frequency is expected to gain intensity at the expense of the regular absorption signal.

After extended exposure to methanol, drastic changes are observed (Fig. 3b, solid symbols). The peak at 1960 cm$^{-1}$

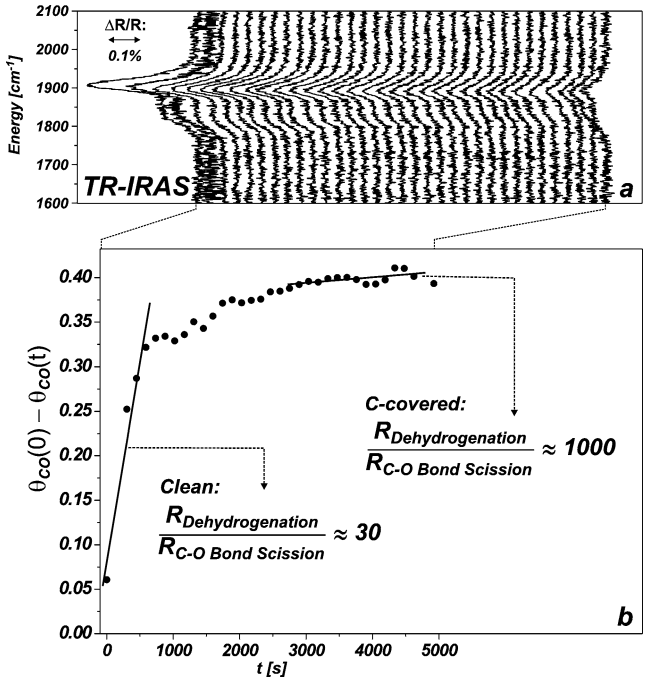


Fig. 4. (a) Time-resolved IR reflection absorption spectra of the CO stretching frequency region during methanol decomposition on $Pd/Al_2O_3/NiAl$ at 440 K; (b) estimated carbon coverage as a function of exposure time to the methanol beam and ratio of the rates of dehydrogenation and C–O bond scission.

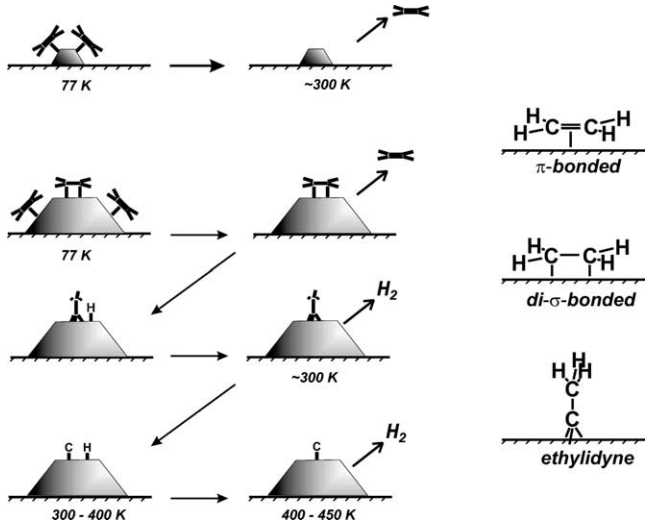


Fig. 5. Schematic representation of the thermal transformation of ethene on Pd particles of different size.

(1) vanishes almost completely, whereas the absorption signal in the on-top region (3) strongly increases (2090 $cm^{-1}$). All other features in the spectrum, in particular the region below 1950 $cm^{-1}$ (regular facets), remain practically unchanged. It is apparent from these observations that adsorption at particle defect sites (i.e., steps and edges) is blocked by carbon species formed via carbon–oxygen bond breakage and thus we conclude that these carbon species preferentially accumulate at defect sites.

In the next step we investigate the effect of carbon accumulation on the kinetics of both reaction pathways. Carbon formation results in a slowly decreasing CO absorption capacity, which allows us to follow the process in situ by TR-RAIRS (Fig. 4a).

In order to quantify the surface fraction covered by carbon we combine a CO sticking coefficient measurement and a TR-RAIRS experiment (Fig. 4a). This calibration is used to estimate the surface fraction covered by carbon ($\theta_C(t) = \theta_{CO}(0) - \theta_{CO}(t)$; $\theta_{CO}(0)$: initial CO coverage) as a function of exposure time to methanol. The result is shown in Fig. 4b. Obviously, the initial rate of carbon formation is high, but drops rapidly with increasing carbon coverage. From this observation we conclude that the carbon–oxygen bond breakage is fast only at the defect sites, which are preferentially blocked during the reaction, but not at the regular facet sites.

The next question to ask is whether the second reaction pathway, i.e., the methanol dehydrogenation, is affected by carbon accumulation in a similar manner. The results of a detailed kinetic molecular beam study involving isotope exchange experiments show that whereas the rate of carbon–oxygen bond breakage drastically decreases with increasing carbon coverage, the rate constant for CO exchange remains nearly unaffected by this process. The decrease in the dehydrogenation rate simply reflects the decrease in the carbon-free Pd surface area. Quantitatively, we find that the ratio between the rates of dehydrogenation and carbon–oxygen bond breakage, $R_{CO}/R_C$, increases from 30 on the pristine sample to approximately 1000 on the carbon-contaminated sample, as indicated in Fig. 4b.

### 3.2. Controlling particle size

Up to this point we have presented evidence for the different activity of various reactive sites coexisting a well-defined supported metal catalyst controlling the selectivity of the reaction.

A second feature of small-particle systems is the dependence of a chemical reaction on the size of the deposited particles, as alluded to in the Introduction. We report here on a study of hydrogenation of ethene in order to investigate the size–reactivity relationship on Pd nanoparticles. It is useful first to recall and summarize the adsorption and dehydrogenation behavior of ethene without the presence of hydrogen.

Combining the results from thermal desorption spectroscopy (TDS) and IRAS [11,53,56], we have proposed a general scheme for ethene thermal transformations on Pd particles, as depicted schematically in Fig. 5. On small Pd particles, ethene is mainly $\pi$-bonded at low temperatures and desorbs intact upon heating. On the larger Pd particles, however, a fraction of the ethene molecules are di-$\sigma$ bonded. Again, weakly bonded ethene desorbs intact (its conversion to di-$\sigma$ species on heating cannot be excluded, however), while di-$\sigma$ ethene can either desorb near room temperature

or dehydrogenate, producing surface species such as ethylidyne and atomic hydrogen. Dehydrogenation proceeds further on heating until a hydrogen-deficient carbonaceous deposit and hydrogen are formed at elevated temperatures. Hydrogen atoms recombine and desorb as hydrogen molecules. Finally, the surface remains covered by carbon deposits at elevated temperatures.

Accordingly, particle size and roughness strongly influence the distribution of $\pi$- and di-$\sigma$ bonded ethene molecules. Due to the development of more extended facets on the large particles, which favor ethene di-$\sigma$ bonding, the reaction pathway shifts toward dehydrogenation and hence to the formation of carbon deposits upon heating.

For pure hydrogen adsorption two adsorption states can be distinguished. One state, leading to desorption around 330 K (called $\beta_2$), is very likely due to hydrogen atoms on the surface of the particles, while a second one desorbing at lower temperatures ($\beta_1$ at $\sim$ 280 K) is tentatively assigned to subsurface hydrogen [57,58]. As a function of particle size, $\beta_2$ shifts to lower temperature with increasing particle size $d$, ranging from 1 nm $< d <$ 5 nm. The formation of the $\beta_1$ state is decreased on the smallest particles, its desorption temperature being less influenced by the size of the particles. This can be a result of the decreasing number of subsurface sites available or due to the presence of the support.

Fig. 6a shows TDS spectra obtained after ethene ($C_2D_4$) adsorption on the clean Pd particles of identical size. We recorded the signals of masses corresponding to $D_2$, $C_2D_4$, and $C_2D_6$. Comparing these spectra, first, we observe the formation of ethane, desorbing at $\sim$ 200 K as the product of ethene hydrogenation. Second, the amount of ethene desorbing at temperatures below 200 K is significantly increased, while the intensity of the state at about 280 K is reduced by a factor of 2. Therefore, the data indicate that it is the formation of di-$\sigma$ ethene that is inhibited by D adatoms. This can be understood by assuming that the surface D atoms, residing presumably in the hollow sites, sterically hinder the di-$\sigma$-bonding. Meanwhile, ethene can readily adsorb onto the D-covered surface via a $\pi$-bond on on-top sites. Therefore, hydrogen preadsorption leads to a redistribution of $\pi$- and di-$\sigma$-bonded ethene, thus favoring a weakly bonded $\pi$-state.

In the reverse experiments, when the Pd particles were ethene precovered before exposure to $D_2$, the spectra were found to be identical to those when there was no $D_2$ exposure at all. This manifests a site-blocking effect of ethene on hydrogen adsorption. Such an effect can be readily explained by the fact that hydrogen dissociation occurs on on-top sites (see review in Ref. [59]), which are occupied by $\pi$-bonded ethene.

In the absence of preadsorbed hydrogen, a very small amount of ethane desorbing at ca. 280 K was detected only for particles larger than 30 Å. This process, called self-hydrogenation, involves the reaction of ethene with hydrogen adatoms produced by dehydrogenation of other ethene molecules. Certainly, such a reaction occurs only on relatively large particles due to an increasing probability of ethene dehydrogenation (see Fig. 5). Nevertheless, the amount of ethane produced by self-hydrogenation is negligibly small as compared to that detected in coadsorption experiments. Moreover, the desorption temperature of ethane formed under coadsorption conditions is about 80 K lower than in a self-hydrogenation reaction (200 K vs 280 K). Such behavior (a temperature shift and an enhanced ethane production) has also been found on hydrogen-precovered Pt(111) [60] and Pd(110) [61] surfaces. Therefore, it appears that a general mechanism of ethene interaction with hydrogen on metal surfaces is valid on both single crystals and small metal particles.

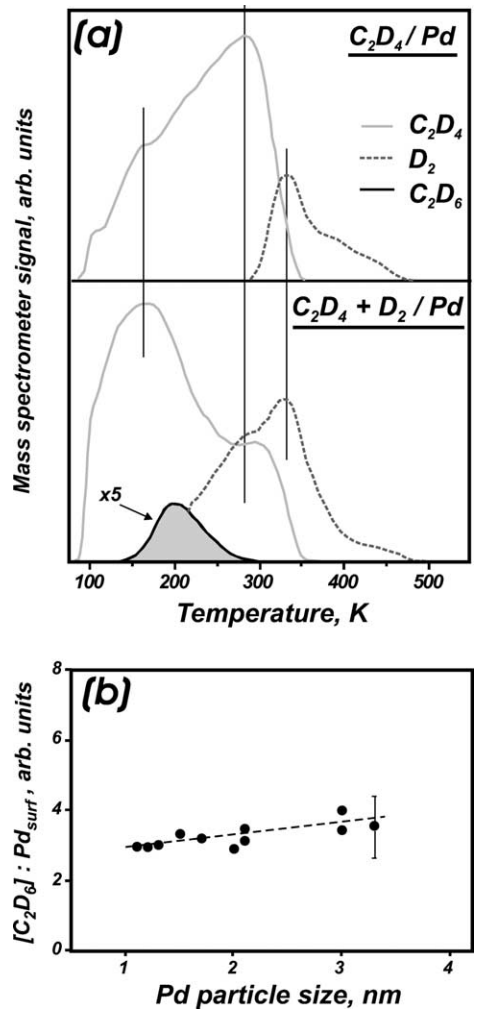


Fig. 6. (a) Thermal desorption spectra of $D_2$, $C_2D_4$ and $C_2D_6$ after exposure of deposited particles of 2 nm average size: (top) 1 L of $C_2D_4$ at 90 K; (bottom) 3 L of $D_2$ at 195 K followed by 1 L of $C_2D_4$ at 90 K. (b) Integrated signal of ethane (shaded in (a) per Pd unit surface area as a function of particle size.

Our TDS study [11] shows that ethene reacts with the most weakly bonded hydrogen present on the surface. The formation of ethane depends on the presence of weakly adsorbed hydrogen, which reacts with $\pi$-bonded ethene before the latter desorbs intact.

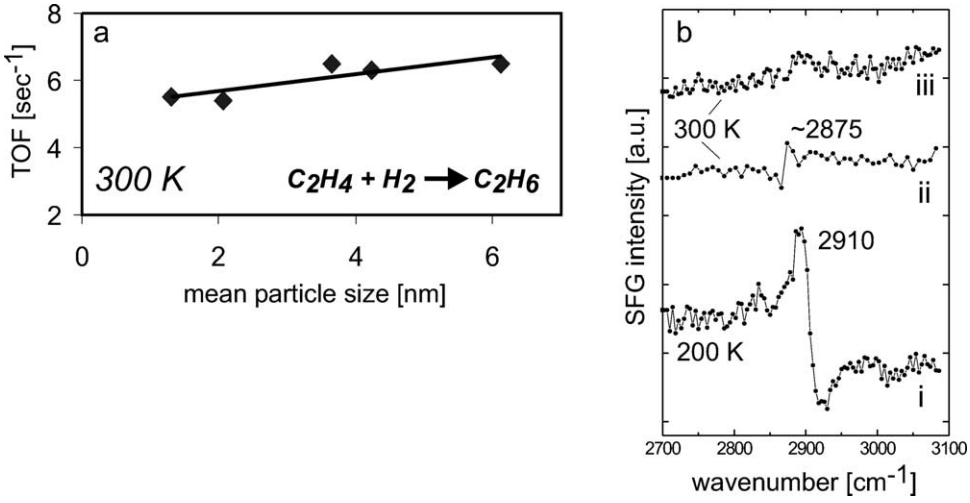


Fig. 7. Ethene hydrogenation activity (a) of $Pd/Al_2O_3/NiAl(110)$ model catalysts with a mean Pd particle size of 1 to 6 nm. The reaction was carried out with 50 mbar $C_2H_4$, 215 mbar $H_2$ and 770 mbar He at 300 K. SFG spectra (b) of $C_2H_4$ on Pd(111) are shown for different conditions: Di-$\sigma$ bonded ethene was observed after saturation at 200 K (i), while a weak signal of ethylidine appeared upon room temperature exposure of ethene (ii). The absence of strong signals (iii) under reaction conditions (5 mbar $C_2H_4$, 5 mbar $H_2$) suggests the presence of $\pi$-bonded ethene [64].

In order to study particle size effects, we have carried out experiments for identical preparations varying only in the amount of deposited Pd, i.e., particle size.

Fig. 6b shows the plot of ethane production per Pd unit surface area as a function of particle size. This plot clearly demonstrates that the hydrogenation activity under the coadsorption conditions studied is almost independent of the Pd particle size in the range 1–3 nm.

Such behavior can be understood by the fact that preadsorbed hydrogen strongly inhibits the formation of di-$\sigma$-bonded ethene and results in preferential formation of the $\pi$-bonded ethene for all particle sizes studied, thus neutralizing the overall particle size influence.

The size independence for ethene hydrogenation obtained in the present work agrees well with the general opinion that this reaction is structure-insensitive [62], and it seems that our system represents a suitable model system for studying the mechanism of the reaction, even using UHV conditions.

The influence of carbonaceous deposits on the particle-size dependence of the ethene hydrogenation reaction has been studied by creating such deposits via dehydrogenation of ethene before exposing the model catalyst to the reaction mixture [63]. It is shown that carbonaceous deposits do not prevent adsorption but inhibit dehydrogenation of di-$\sigma$-bonded ethene. Using CO as a probe molecule, it can be shown that the carbon deposits occupy highly coordinated sites on the surface. Ethene hydrogenation is inhibited by the presence of carbon deposits but the inhibition is independent of particle size in the range studied (1–3 nm).

Clearly, the results reported for ethene hydrogenation have been obtained under ultra-high-vacuum conditions and the question currently asked is, are the results compatible with results under realistic reaction conditions? We have exposed the same model catalyst as studied above to ambient conditions and measured turnover frequencies (TOF) via gas chromatography as typically done in a catalytic study [13]. At the same time, we can follow the species on the surface with in situ vibrational spectroscopy, namely sum-frequency generation (SFG) that allows us to measure vibrational spectra in the presence of a gas phase. The latter method has been reviewed recently by Rupprechter [19] and applied to nanoparticle model catalysts by Dellwig et al. [17].

Fig. 7 shows turnover frequencies as a function of particle size measured on model catalysts prepared in the same way as used for the ultra-high-vacuum studies [13,63,64]. The model catalyst was placed in a reaction vessel [65] and exposed to a mixture of $C_2H_4$ (50 mbar), $H_2$ (215 mbar), and He (770 mbar), with ethane production being monitored by on-line gas chromatography at various temperatures and reaction times [13]. Knowing the structure and morphology of the catalyst, turnover frequencies are calculated. The system turned out to be stable under reaction. The TOFs are rather independent of particle size and the activation energy for ethene hydrogenation from temperature-dependent data is ca. 55 kJ/mol [13]. There is a remarkable correspondence of particle-size-dependent properties under ultrahigh vacuum and ambient conditions, which already at this stage can be taken as indication that the mechanisms are similar under both conditions. SFG spectroscopy can be applied as an in situ technique during reactions and spectra on Pd(111) as a model surface are also shown in Fig. 7b [64]. To identify the species involved, UHV adsorption studies were initially performed (Fig. 7b, curves I and ii). At 200 K, a characteristic spectrum of di-$\sigma$-bonded ethene was observed, while $\pi$-bonded ethene shows no signal due to its parallel geometry on the (111) surface (with C–H bonds still being in plane). At 300 K, a small signal from ethylidyne appeared due to ethene decomposition. Under reaction conditions (Fig. 7b, curve iii), no distinct signals are observed, suggesting that di-$\sigma$-bonded ethene and ethylidyne are not turning over and

that, rather, $\pi$-bonded ethene is the active species. The SFG spectra provide considerable indirect evidence for this conclusion. Experiments are being performed to try to clarify this issue. Therefore, so far, indications are that the species turning over under realistic conditions is the same as under ultra-high-vacuum conditions.

In summary, we have presented an example where a simple reaction has been studied under both ambient and ultra-high-vacuum conditions, and it is shown that the results parallel each other to a large extent, so that ideas can be transferred between the two regimes. This is certainly a feature that is connected with the specific system and reaction under investigation and one has to check from system to system whether transferability is given. On the other hand, it is clear that there are cases where reaction mechanisms and structure in both regimes are the same. There is accumulating evidence that this may be the case for several systems. The example also illustrates the necessity to further develop in situ spectroscopic techniques.

## 4. Heterogenized homogeneous model catalysts: Ziegler–Natta low pressure ethene polymerization

The following example represents another case where the application of in situ techniques to model catalysts allow a detailed view of molecular processes in a reaction at surfaces.

Transition metal (in particular titanium) halides and organoaluminum compounds have been in use since Ziegler's early work in the early 1950s [66] to (homogeneously) catalyze the polymerization of ethene [67,68]. With the extension of Ziegler's work by Natta et al. [69,70] to use these systems in the synthesis of stereo regular poly($\alpha$)alkenes, the basis for more than 10% of all profits made with organometallic catalysts was laid [71]. Since the development of the first generation Ziegler–Natta catalysts, several generations of such catalysts have been put in place which exhibit activity and efficiency orders of magnitude higher [68]. The third generation of Ziegler–Natta catalysts actually represents a supported catalyst which has been developed and used since 1975 to increase the amount of active Ti using inorganic chlorides, such as $MgCl_2$ and $CoCl_2$, as supports [72]. The high activity of these catalysts permitted the use of low catalyst concentrations and, therefore, catalyst residues can remain in the polymer [68]. The literature on the topic of Ziegler–Natta catalysis is huge and still growing since the development of the new generation of metallocene/methylaluminoxane catalysts has recently increased interest in this field substantially [67,73–75]. There are several excellent reviews on the subject and we refer to one by Kaminski and Arndt [68], in particular.

Interesting and important contributions to our understanding have recently been gained through theoretical studies by Parrinello and his group, e.g., [76].

The experimental characterization of supported third generation Ziegler–Natta catalysts has been mainly done indirectly in the past via polymer product analysis. However, knowledge of surface properties of such systems is of fundamental importance to describe the process and its mechanism in detail. Surface science studies on polymerization catalysts are rather scarce. Model studies on the Phillips catalyst have been performed [77,78] and, most importantly, Somorjai and co-workers [79–84] published a series of papers on the preparation and characterization of model systems for supported Ziegler–Natta catalysts. These model systems have been used to polymerize ethene.

Following the work of Somorjai and co-workers [79–84], we have used a model system consisting of an epitaxially grown $MgCl_2$ film onto which $TiCl_4$ was anchored as the active component. The anchoring process has been studied by electron spectroscopy [83] and, recently in our group, by ESR spectroscopy; we have shown that surface defects in the $MgCl_2$ film are crucial in this process [16]. The key step, however, is the so-called activation of the system by adding a co-catalyst, namely an alkyl aluminum compound (trimethylaluminum (TMA), triethylaluminum (TEA)). In this process is it believed that Ti ions assume a lower oxidation state and when TMA is used radicals ($R^{\bullet}$) are created according to Eq. (1), whereas the activation with TEA takes place through a disproportionation reaction [85–87].

ESR spectroscopy as another in situ technique can be favorably used to prove the formation of radicals according to

$$TiCl_4 + AlR_3 \rightarrow RTiCl_3 \rightarrow TiCl_3 + R^{\bullet}. \quad (1)$$

In Fig. 8 the preparation of the model system is briefly summarized. A Pd(111) substrate is covered by a $MgCl_2$ film in the (001) orientation. It grows in a layer-by-layer mode and the surface is terminated by chloride ions, as shown by LEED and Auger spectroscopy.

Magni and Somorjai, in their pioneering work, already realized that it is necessary to produce defects in the film to bind the $TiCl_4$ precursor [79–83,88]. The idea really goes back even further [89,90], however. Early on it was noted that the uncoordinated edge and corner sites on a $MgCl_2$ crystallite bind $TiCl_4$ [67,72,91], as is also corroborated by recent model calculations [76,92].

There are several ways to produce defect-containing surfaces. One way is to keep the Pd(111) surface temperature low, so that the mobility of the $MgCl_2$ is too low to produce a fully epitaxial film. However, the problem here is that such films often contain pinholes, which change the reactivity of the system. Therefore, first creating a fully epitaxial film and then producing defects by either electron or ion bombardment has been considered [79–83,88]. Fig. 9 compares the ESR spectra for the two cases, namely defects created at lower growth temperature (bottom) and after sequential bombardment with electrons and argon ions.

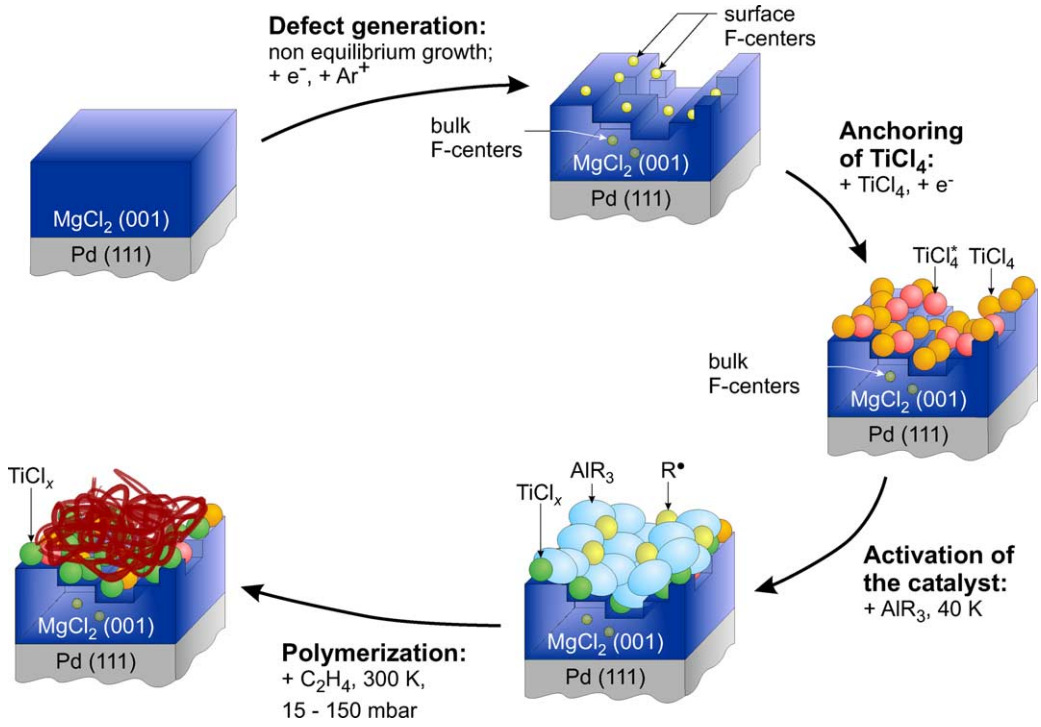


Fig. 8. Schematic representation of the preparation of the Ziegler–Natta model catalyst.

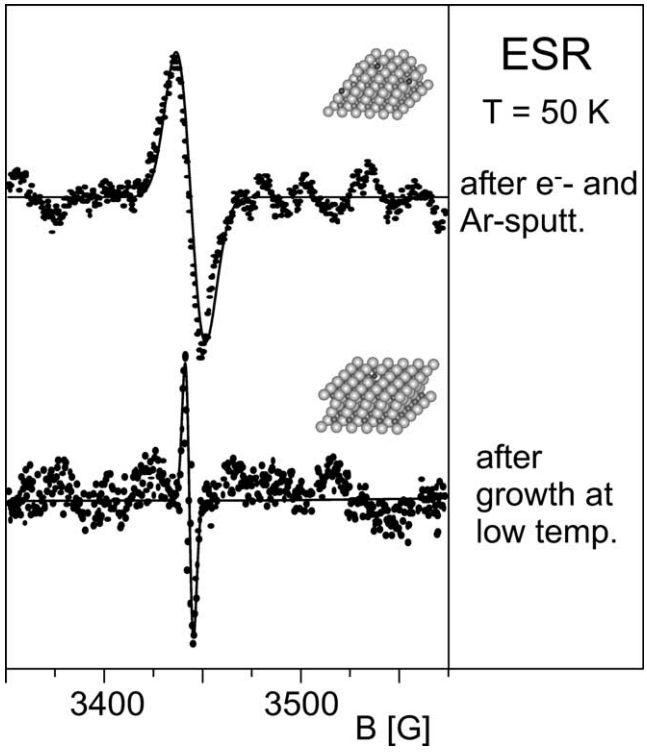


Fig. 9. ESR spectra of color centers in a $MgCl_2$ film for two different preparation conditions: (top) an initially well-ordered film after bombardment with electrons and argon ions; (bottom) film grown at lower temperatures. Insets sketch the different environments of surface color centers for both situations.

Let us first consider the nonepitaxial film. Both, the position of the band in the lowest trace and the temperature dependence, which is Curie-like, favor the formation of color centers, i.e., removal of a Cl atom which leaves an unpaired electron behind. For a more detailed discussion of color centers we resort to the work of Giamello et al. on color centers [93]. The position of the present signal is close to that observed for color centers in MgO single crystals. Part of the ESR spectrum (40%) is quenched upon adsorption of $TiCl_4$, which suggests that they are located at the surface of the film.

If we grow an epitaxial film as done for the upper trace, there is no detectable ESR signal before further treatment of the film, which leads to a sharp LEED pattern with low background intensity. Bombardment of the film with electrons or argon ions does disturb the structure, as judged by the background of the LEED picture as well as Auger spectroscopy, which shows a loss of chlorine, especially for the electron-induced process. However, none of these processes alone is sufficient to create an ESR active defect. Subsequent argon ion bombardment (150 eV, 1 $\mu A/cm^2$, 3 min) of a sample initially exposed to electrons does produce an ESR signal, as shown in the upper trace, Fig. 9. As compared to the spectra of the defects created by growth at lower temperatures the signal is shifted to higher $g$-values. Additionally, the linewidth increases from 4 to 14 G. This might be explained by the creation of color centers on the rough surface exposing different low coordinated sites, which will have slightly different $g$-values than the color center on the (001) terrace. This geometric situation of the color centers is sketched in Fig. 9.

$TiCl_4$ has a high enough vapor pressure to dose the molecule from the gas phase. Adsorption of $TiCl_4$ and subsequent electron bombardment leads to the formation of $Ti^{3+}$ centers, as monitored by ESR. Depending on the preparation conditions, two cases can be distinguished. For films showing the signature of paramagnetic color centers in the ESR a broad signal situated at $g = 1.93$ is found, whereas films without paramagnetic defects exhibit a much sharper feature centered at $g = 1.96$. However, there is no indication that the presence of the observed $Ti^{3+}$ signals correlates with the polymerization activity of the catalyst. The $g$-values found are situated among values reported for $TiCl_3$ in octahedral ($g = 1.94$) and tetrahedral ($g = 1.97$) environments [94–96]. These values have been measured for Ziegler–Natta catalysts, but also in those cases there is no clear indication for a correlation with the catalyst activity. While the signal observed on the surface with fewer defects is close to the value observed for tetrahedral environments, the signal of the surface showing paramagnetic defects is centered at the value for octahedral environments. Comparing the linewidth of the signals measured here with the ones in the literature, the general trend of the signal at $g = 1.94$ being broader than the ones at $g = 1.97$ holds true also for these measurements; however, the linewidth of the resonance at $g = 1.93$ is considerably broadened as compared to the literature. Considering the stronger disorder of these systems, it is more likely that isolated $Ti^{3+}$ centers are formed in this case, which may comprise different local environments and thus show a larger linewidth. The lack of an ESR signal corresponding to $Ti^{3+}$ ions in cases where no additional argon or electron bombardment has been applied cannot be interpreted as a clear indication of the absence of $Ti^{3+}$ at the surfaces. In the literature there are discussions that small spin-lattice relaxation times, dipole coupling, and super exchange may only leave a very small fraction of $Ti^{3+}$ ESR active or detectable due to increase in linewidth [97,98].

The $TiCl_4/MgCl_2$ system is, as it is called in Ziegler–Natta catalysis, activated by exposing it to the co-catalyst, i.e., an aluminum alkyl compound. We have used trimethylaluminum (TMA) and triethylaluminum (TEA) for activation. The compounds have been dosed from the gas phase either at room temperature for a prolonged time or at 40 K surface temperature for a much shorter time. Typically, 3400 L of TMA or TEA was exposed. The infrared spectrum of the condensed film showed the typical FTIR spectrum known from condensed and matrix isolated species [99]. There are bands that can be assigned to dimeric aluminum alkyl species.

Fig. 10 shows ESR spectra after reaction of the TMA with the $TiCl_4/MgCl_2$ system [14]. A typical low coverage of $TiCl_4$ leads to the spectra shown in the upper trace. Increasing the amount of $TiCl_4$ on the surface by a factor of 3 increases the intensity of the ESR spectrum by a factor of 1.7, which indicates that the number of surface titanium centers increases with the total amount of titanium on the surface. This can be understood by means of an island-like

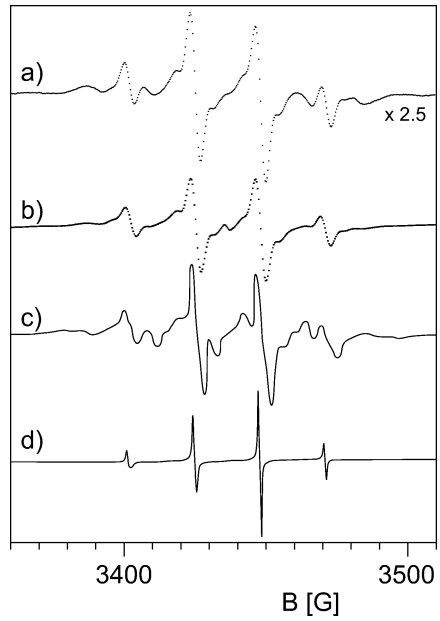


Fig. 10. ESR spectra of alkyl radicals (a) after adsorption of $AlMe_3$ at 40 K on a model catalyst. Spectrum is enlarged by a factor of 2.5 as compared to (b). (b) Equivalent procedure to (a), for a catalyst containing a threefold higher titanium content as compared to (a). (c) Ethyl radicals in an ethyl chloride matrix at 77 K [103]. (d) Methyl radicals on a silica surface at 77 K [102].

growth mode of $TiCl_4$ on the surface. The spectrum is free of any $Ti^{3+}$ signal. This is in accordance with the observation in the literature of the formation of mainly $Ti^{2+}$ species due to the reduction with aluminum alkyls [100,101]. Although it might be thought that methyl radicals are the most natural products in the reduction of a mixed titanium–chlorine–methyl species, a comparison of the line shape of the observed spectra with spectra of methyl radicals (shown at the bottom of Fig. 10) taken from the literature [102] clearly shows that the species present here are not methyl radicals. Whereas the ESR spectrum of a methyl radical is a quartet of lines, the spectrum observed here, though dominated by a quartet structure, shows a couple of additional lines, pointing to additional interactions of the unpaired electron. By comparing the lineshape to other alkyl radicals it turned out that the present spectrum can be attributed to ethyl radicals. Fig. 10 shows for comparison ethyl radicals created in an ethylchloride matrix generated by photolysis [103]. The lineshape of the ethyl radicals can be understood by assuming that the protons of the methyl group adjacent to the spin containing the methylene group, which cause hyperfine interaction with the unpaired electron, are magnetically equivalent due to a fast rotation of the methyl group along the C–C bond. The two protons of the methylene group, however, give rise to anisotropic superhyperfine interaction because the adsorption of the molecule on the surface hinders the rotation of the molecule in space. Assuming the anisotropic interaction to be axially symmetric allows a good description of the observed lineshape, as shown by Shiga et al. [102].

There are two key questions that have to be answered.

1. How have the $C_2H_5$ radicals been created?
2. Have the radicals been created at the TMA/$TiCl_4$–$MgCl_2$ interface or in the TMA activating materials?

The second question can be answered by studying the number of radicals formed as a function of the amount of $TiCl_4$ at the interface and as a function of exposed TMA. As a function of $TiCl_4$ the ESR intensity increases for a low $TiCl_4$ concentration regime, but it shows clear saturation behavior, when plotted versus the amount of TMA adsorbed. Both observations are compatible with a radical creation process at the TMA–$TiCl_4/MgCl_2$ interface, where alkylation of the $TiCl_4$ by ligand exchange is supposed to occur. Assuming this ligand exchange to occur, the primary radical that can be created is a methyl radical. For this radical there are several possibilities for consecutive reactions given the size and high mobility, even at low temperature, in the solid state [104].

The most likely reaction yielding ethyl radicals is

$$CH_3\bullet + Al(CH_3)_3 \rightarrow H_3C\text{–}H_2C\bullet + AlH(CH_3)_2.$$

Even though such a reaction has not been investigated so far it can be crudely estimated that it is energetically possible. Above 50 K the intensity of the ethyl radicals is attenuated irreversibly and decreases below the detection limit above 80 K. This can be explained by assuming the ethyl radicals to diffuse and recombine at these temperatures, as has been observed for methyl radicals above 45 K [105] and $NO_2$ radicals on an oxide surface above 75 K [20].

After unreacted TMA has all been desorbed, carbon due to the successful alkylation of the $TiCl_4$ is still found on the surface. It is, however, important to note that after removal of the reacted $TiCl_x$ moieties from the surface, e.g., by soft argon sputtering, and redosing with TMA, new $C_2H_5$ radicals can be created.

An interesting observation is made if TEA is used instead of TMA. Even though the catalyst can be activated in a way similar to TMA, radicals created from TEA have never been observed. This is in line with expectations from the literature because here a disproportionation has been proposed according to:

$$AlEt_3 + TiCl_4 \rightarrow AlEt_2Cl + TiCl_3Et,$$

$$2TiCl_3Et \rightarrow 2TiCl_3 + C_2H_4 + C_2H_6.$$

Because ethyl radicals have been observed in the preceding experiment, which also suggest that these radicals are stable at the given temperature, the initial formation of ethyl radicals would undoubtedly lead to observation of the radicals. The absence of an ESR spectrum therefore strongly suggests a disproportionation reaction in accordance with the interpretation in the literature from indirect evidence [85–87,106].

The model catalyst was exposed to ethylene at 15 to 150 mbar; the gas was introduced into the IR chamber through the gas-dosing system. Fig. 11 shows the IR spectrum of the generated polyethylene. Characteristic are the stretching modes at 2852/2924 $cm^{-1}$, the doublets of the deformation modes at 1473/1463 $cm^{-1}$, and the rocking modes at 730/720 $cm^{-1}$. In comparison with the literature the observed frequencies of the stretching modes are situated at the higher end for dominating *trans*-configurations. This was taken as an indication that the polymer chains have long-range order in *trans*-configurations but also contain some *gauche* defects.

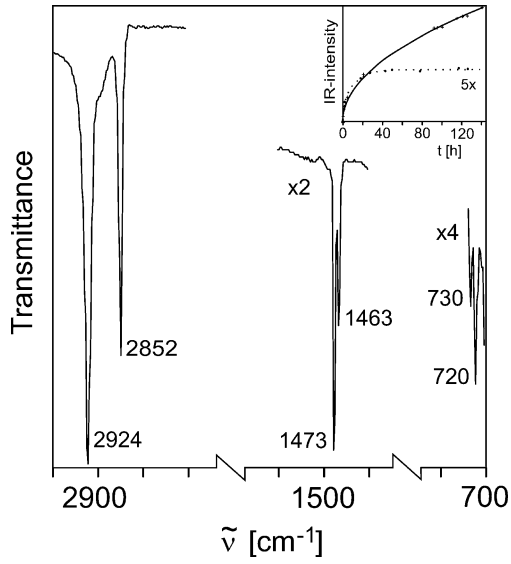


Fig. 11. IR spectrum of polyethylene polymerized on the model catalyst. (Inset shows kinetics of the ethylene polymerization at 300 K as measured by IR spectroscopy. The full line represents the kinetics measured for a rough catalyst; the kinetics of a smooth catalyst with fewer defects is indicated by the dotted line.)

The course of the reaction has been studied by evaluating the IR band at 2852 $cm^{-1}$, which is the one least influenced by the presence of gaseous ethylene. The polymerization has been followed for 12 to 150 h.

Two different kinds of behavior have been observed. Typical results are given in the inset of Fig. 11. The determining factor is here the degree of disorder in the surface of the model catalyst. While a catalyst with a high degree of disorder shows a monotonic increase of the polyethylene amount with time, catalysts prepared on a smooth surface with fewer defects show a self-terminating reaction after approximately 50 h, leading to film considerably less thick than the former case. This can be explained in a straightforward way by considering that on a smooth surface a rather smooth polymer film forms, which in a relatively short time becomes impermeable to ethylene from the gas phase, so that the reaction is self-limiting. In the other case, the growing film possibly has a sufficient number of pores so that the monomer can continue to reach the catalyst and the reaction keeps going. This assumes that the polymerization reaction takes place at the interface of the polymer and the magnesium chloride support, which has been recently corroborated experimentally [107]. The latter behavior can be modeled by assuming

that the monomer molecules are transported by diffusion to the interface. The amount of polymer, $n_e$, increases with reaction time $t$ according to

$$n_e = \delta\sqrt{t},$$

where the constant $\delta$ is a function of the diffusion coefficient, the surface area, the molar volume of the polymer and the concentration at infinite time $t$.

Therefore, we expect that the IR intensity increases as $\sqrt{t}$. With $\delta = 4.6 \times 10^{-2}$ mol s$^{-1/2}$ the fit given in Fig. 11 has been obtained. In conclusion, a combination of ESR and IRAS allows us to follow the polymerization of ethene in some detail.

## 5. Synopsis

This brief overview was intended to demonstrate that studies on model catalyst systems can lead to a rather detailed understanding of processes involved in the complex operation of heterogeneous and heterogenized homogeneous catalysts. Of course, this work represents only two case studies and one cannot generalize the findings at this point. However, by combining model systems of increasing complexity with in situ spectroscopic methods, such as sum frequency generation and ESR spectroscopy, employed in the studies described here, it can be foreseen that useful new solid information on model systems under reaction conditions may be extracted that will bring us closer to in closing the gaps between catalysis and surface science. In the future the complexity of model systems will increase. For example, oxide particles grown on oxide supports are the focus of several groups. A close look at kinetics on such systems is likely to be possible using molecular beam and other standard methods employing gas-chromatographic ms techniques over the entire pressure range from UHV to 1 bar.

## References

[1] M. Che, C.O. Bennet, Adv. Catal. 20 (1989) 153.
[2] G. Ertl, H. Knözinger, J. Weitkamp (Eds.), Handbook of Heterogeneous Catalysis, Wiley–VCH, Weinheim, 1997, pp. 1560–2122.
[3] P.L.J. Gunter, J.W.H. Niemantsverdriet, F.H. Ribeiro, G.A. Somorjai, Catal. Rev. Sci. Eng. 39 (1997) 77.
[4] C.R. Henry, Surf. Sci. Rep. 31 (1998) 231–326.
[5] C.T. Campbell, Surf. Sci. Rep. 27 (1997) 1–111.
[6] D.W. Goodman, Surf. Rev. Lett. 2 (1995) 9.
[7] U. Diebold, J.-M. Pan, T.E. Madey, Surf. Sci. 331–333 (1995) 845.
[8] H.-J. Freund, Angew. Chem. Int. Ed. Engl. 36 (1997) 452–475.
[9] H.-J. Freund, Surf. Sci. 500 (2002) 271.
[10] H.-J. Freund, M. Bäumer, H. Kuhlenbeck, Adv. Catal. 45 (2000) 333–384.
[11] S.K. Shaikhutdinov, M. Heemeier, M. Bäumer, T. Lear, D. Lennon, R.J. Oldman, S.D. Jackson, H.-J. Freund, J. Catal. 200 (2001) 330.
[12] S. Schauermann, J. Hoffmann, V. Johanek, J. Hartmann, J. Libuda, H.-J. Freund, Angew. Chem. Int. Ed. 41 (2002) 2532.
[13] G. Rupprechter, H. Unterhalt, M. Morkel, P. Galletto, L. Hu, H.-J. Freund, Surf. Sci. 502–503 (2002) 109.
[14] T. Risse, J. Schmidt, H. Hamann, H.-J. Freund, Angew. Chem. Int. Ed. Engl. 41 (2002) 1518.
[15] M. Bäumer, H.-J. Freund, Progr. Surf. Sci. 61 (1999) 127.
[16] J. Schmidt, T. Risse, H. Hamann, H.-J. Freund, J. Chem. Phys. 116 (2002) 10861.
[17] T. Dellwig, G. Rupprechter, H. Unterhalt, H.-J. Freund, Phys. Rev. Lett. 85 (2000) 776.
[18] H. Unterhalt, G. Rupprechter, H.-J. Freund, J. Phys. Chem. B 106 (2002) 356.
[19] G. Rupprechter, Phys. Chem. Chem. Phys. 3 (2001) 4621.
[20] H. Schlienz, M. Beckendorf, U.J. Katter, T. Risse, H.-J. Freund, Phys. Rev. Lett. 74 (1995) 761–764.
[21] U.J. Katter, H. Schlienz, M. Beckendorf, H.-J. Freund, Ber. Bunsenges. Phys. Chem. 97 (1993) 340.
[22] U. Heiz, F. Vanolli, L. Trento, W.D. Schneider, Rev. Sci. Instrum. 68 (1997) 1986.
[23] H.-J. Freund, Phys. Status Solidi B 192 (1995) 407–440.
[24] D.W. Goodman, J. Vac. Sci. Technol. A 14 (1996) 1526.
[25] T. Schröder, M. Adelt, B. Richter, M. Naschitzki, M. Bäumer, H.-J. Freund, Surf. Rev. Lett. 7 (2000) 7–14.
[26] T. Schröder, J. Giorgi, M. Bäumer, H.-J. Freund, Phys. Rev. B, in press.
[27] R.M. Jaeger, H. Kuhlenbeck, H.-J. Freund, M. Wuttig, W. Hoffmann, R. Franchy, H. Ibach, Surf. Sci. 259 (1991) 235.
[28] J. Libuda, F. Winkelmann, M. Bäumer, H.-J. Freund, T. Bertrams, H. Neddermeyer, K. Müller, Surf. Sci. 318 (1994) 61.
[29] P. Gassmann, R. Franchy, H. Ibach, Surf. Sci. 319 (1994) 95.
[30] R. Franchy, J. Masuch, P. Gassmann, Appl. Surf. Sci. 93 (1996) 317.
[31] U. Bardi, A. Atrei, G. Rovida, Surf. Sci. 268 (1992) 87.
[32] C. Becker, J. Kandler, H. Raaf, R. Linke, T. Pelster, M. Dräger, M. Tanemura, K. Wandelt, J. Vac. Sci. Technol. A 16 (1998) 1000.
[33] H. Graupner, L. Hammer, K. Heinz, D.M. Zehner, Surf. Sci. 380 (1997) 335.
[34] C. Uebing, Ber. Bunsenges. Phys. Chem. 102 (1998) 1156.
[35] J. Libuda, M. Frank, A. Sandell, S. Andersson, P.A. Brühwiler, M. Bäumer, N. Mårtensson, H.-J. Freund, Surf. Sci. 384 (1997) 106–119.
[36] S. Stempel, M. Bäumer, H.-J. Freund, Surf. Sci. 402–404 (1998) 424–427.
[37] M. Heemeier, PhD thesis, Freie Universität Berlin, Berlin, in preparation.
[38] N. Ernst, B. Duncombe, G. Bozdech, M. Naschitzki, H.-J. Freund, Ultramicroscopy 79 (1999) 231.
[39] A. Piednoir, E. Perrot, S. Granjeaud, A. Humbert, C. Chapon, C.R. Henry, Surf. Sci. 391 (1997) 19–26.
[40] K.H. Hansen, T. Worren, S. Stempel, E. Lægsgaard, M. Bäumer, H.-J. Freund, F. Besenbacher, I. Stensgaard, Phys. Rev. Lett. 83 (1999) 4120–4123.
[41] G.A. Kok, A. Noordermeer, B.E. Nieuwenhuys, Surf. Sci. 135 (1983) 65.
[42] R.P. Holroyd, M. Bowker, Surf. Sci. 377–379 (1997) 786.
[43] M. Rebholz, N. Kruse, J. Chem. Phys. 95 (1991) 7745.
[44] J.-J. Chen, Z.-C. Jiang, Y. Zhou, B.R. Chakraborty, N. Winograd, Surf. Sci. 328 (1995) 248.
[45] M.P. D'Evelyn, R.J. Madix, Surf. Sci. Rep. 3 (1984) 413.
[46] M. Asscher, G.A. Somorjai, in: G. Scoles (Ed.), Atomic and Molecular Beam Methods, Oxford Univ. Press, Oxford, 1988, p. 489.
[47] J. Libuda, H.-J. Freund, J. Phys. Chem. B 106 (2002) 4901.
[48] J. Libuda, I. Meusel, J. Hartmann, H.-J. Freund, Rev. Sci. Instrum. 71 (2000) 4395.
[49] J. Libuda, I. Meusel, J. Hoffmann, J. Hartmann, M. Piccolo, C.R. Henry, H.-J. Freund, J. Chem. Phys. 114 (2001) 4669.
[50] I. Meusel, J. Hoffmann, J. Hartmann, J. Libuda, H.-J. Freund, J. Phys. Chem. B 105 (2001) 3567.
[51] V. Matolin, M. Rebholz, N. Kruse, Surf. Sci. 245 (1991) 233.
[52] K. Wolter, O. Seiferth, H. Kuhlenbeck, M. Bäumer, H.-J. Freund, Surf. Sci. 399 (1998) 190–198.
[53] M. Frank, M. Bäumer, Phys. Chem. Chem. Phys. 2 (2000) 3723.
[54] F.M. Hoffmann, Surf. Sci. Rep. 3 (1983) 107.

[55] P. Hollins, Surf. Sci. Rep. 16 (1992) 51.
[56] M. Frank, M. Bäumer, R. Kühnemuth, H.-J. Freund, J. Vac. Sci. Technol. A 19 (2001) 1497–1501.
[57] H. Okuyama, W. Siga, N. Takagi, M. Nishijima, T. Aruga, Surf. Sci. 401 (1998) 344.
[58] D. Farias, M. Patting, K.H. Rieder, Phys. Status Solidi 159 (1997) 255.
[59] K. Christmann, in: Z. Paal, P.G. Menon (Eds.), Hydrogen Effects in Catalysis, Dekker, New York, 1988, p. 3.
[60] D. Godbey, F. Zaera, R. Yeates, G.A. Somorjai, Surf. Sci. 167 (1986) 150.
[61] T. Sekitani, T. Takaoka, M. Fujisawa, M. Nishijima, J. Phys. Chem. 96 (1992) 8462.
[62] G.A. Somorjai, Introduction to Surface Chemistry and Catalysis, Wiley, New York, 1994.
[63] S. Shaikhutdinov, M. Frank, M. Bäumer, S.D. Jackson, R.J. Oldman, J.C. Hemminger, H.-J. Freund, Catal. Lett. 80 (2002) 125.
[64] G. Rupprechter, H. Unterhalt, L. Hu, H.-J. Freund, in preparation.
[65] G. Rupprechter, T. Dellwig, H. Unterhalt, H.-J. Freund, Top. Catal. 15 (2001) 19.
[66] K. Ziegler, E. Holzkamp, H. Martin, H. Breil, Angew. Chem. 67 (1955) 541.
[67] P.C. Barbé, G. Cecchin, L. Noristi, Adv. Polym. Sci. 81 (1987) 1.
[68] W. Kaminsky, M. Arnott, in: G. Ertl, H. Knözinger, J. Weitkamp (Eds.), Handbook of Heterogeneous Catalysis, Wiley–VCH, Weinheim, 1997, p. 2405.
[69] G. Natta, J. Polym. Sci. 16 (1955) 143.
[70] G. Natta, P. Pino, P. Mazzanti, US Patent 3,715,344, 1954.
[71] G. Fink, R. Mühlhaupt, H.H. Brintzinger (Eds.), Ziegler Catalysts, Springer, Heidelberg, 1994.
[72] J.J.A. Dusseault, C.C. Hsu, J. Macromol. Sci. Rev. Macromol. Chem. Phys. C 33 (1993) 103.
[73] M.R. Mason, J. Am. Chem. Soc. 115 (1993) 4971.
[74] C.J. Harlan, M.R. Mason, A.R. Barron, Organometallics 13 (1994) 2957.
[75] H. Sinn, Macromol. Symp. 97 (1995) 27.
[76] M. Boero, M. Parrinello, H. Weiss, S. Hüfter, J. Phys. Chem. A 105 (2001) 5096.
[77] I. Hemmerich, F. Rohr, O. Seiferth, B. Dillmann, H.-J. Freund, Z. Phys. Chem. 202 (1997) 31–43.
[78] P.C. Thüne, J. Loos, P.J. Lemstra, H. Niemantsverdriet, J. Catal. 183 (1999) 1.
[79] E. Magni, G.A. Somorjai, Appl. Surf. Sci. 89 (1995) 187.
[80] E. Magni, G.A. Somorjai, Catal. Lett. 35 (1995) 205.
[81] E. Magni, G.A. Somorjai, Surf. Sci. 345 (1996) 1.
[82] E. Magni, G.A. Somorjai, J. Phys. Chem. 100 (1996) 14786.
[83] T.A. Korányi, E. Magni, G.A. Somorjai, Top. Catal. 7 (1999) 179.
[84] S.H. Kim, G.A. Somorjai, Appl. Surf. Sci. 161 (2000) 333.
[85] U. Thewalt, Gmelins Handbuch der anorganischen Chemie, Springer, Heidelberg, 1977.
[86] H. de Vries, Rec. Trav. Chim. 80 (1961) 866.
[87] C. Beermann, H. Bestian, Angew. Chem. 71 (1959) 618.
[88] E. Magni, G.A. Somorjai, Surf. Sci. Lett. 341 (1995) L1078.
[89] P. Galli, P.C. Barbé, G. Guidetti, R. Zannetti, A. Marigo, M. Bergozza, A. Fichera, Eur. Polym. J. 19 (1983) 19.
[90] R. Gerbasi, A. Marigo, A. Martorana, R. Zannetti, G. Guidetti, G. Baruzzi, Eur. Polym. J. 20 (1984) 967.
[91] P. Corradini, G. Guerra, Polym. Sci. 16 (1991) 239.
[92] C. Martinsky, C. Minot, J.M. Ricart, Surf. Sci. 490 (2001) 237.
[93] E. Giamello, D. Murphy, L. Ravera, S. Coluccia, A. Zecchina, J. Chem. Soc. Faraday Trans. 90 (20) (1994) 3167.
[94] J. Peyroche, Y. Girard, R. Laputte, A. Guyot, Makromol. Chem. 129 (1969) 215.
[95] K. Soga, M. Terano, Makromol. Chem. 182 (1981) 2439.
[96] V.A. Zakharov, S.I. Makhtarulin, V.A. Poluboyraov, V.F. Anufrienko, Makromol. Chem. 185 (1984) 1781.
[97] J.C.W. Chien, J.C. Wu, J. Polym. Sci. Polym. Chem. Ed. 20 (1982) 2461.
[98] H. Fuhrmann, W. Herrmann, Macromol. Chem. Phys. 195 (1994) 3509.
[99] S. Kvisle, E. Rytter, Spectrochim. Acta 40 (10) (1984) 939.
[100] E. Magni, G.A. Somorjai, Surf. Sci. 377–379 (1997) 824.
[101] S.H. Kim, G.A. Somorjai, J. Phys. Chem. B 105 (2001) 3922.
[102] T. Shiga, H. Yamaohu, A. Lund, Z. Naturforsch. A 29 (1974) 653.
[103] P.B. Ayscough, C. Thomson, Trans. Faraday Soc. 58 (1962) 1477.
[104] R.L. Morehouse, J.J. Christiansen, W. Gordy, J. Chem. Phys. 45 (5) (1966) 1751.
[105] K. Toriyama, M. Iwasaki, K. Nunome, J. Chem. Phys. 71 (4) (1979) 1968.
[106] F.S. D'yachowvskii, N.E. Khrushch, A.E. Shilov, Kinet. Katal. (USSR) 9 (1968) 831.
[107] S.H. Kim, G.A. Somorjai, Catal. Lett. 68 (2000) 7.
[108] I. Meusel, J. Hoffmann, J. Hartmann, M. Heemeier, M. Bäumer, J. Libuda, H.-J. Freund, Catal. Lett. 71 (2001) 5.